Lattice dynamics and heat transport in zeolitic imidazolate framework glasses

Yuan, Chengyang; Sørensen, Søren Strandskov; Du, Tao; Zhang, Zhongyin; Song, Yongchen; Shi, Ying; Neuefeind, Jörg; Smedskjær, Morten Mattrup

Published in:
Journal of Chemical Physics

DOI (link to publication from Publisher):
10.1063/5.0196613

Publication date:
2024

Document Version
Accepted author manuscript, peer reviewed version

Lattice dynamics and heat transport in zeolitic imidazolate framework glasses

Chengyang Yuan[1,2], Søren S. Sørensen[1], Tao Du[1], Zhongyin Zhang[3], Yongchen Song[2], Ying Shi[4], Jörg Neuefeind[5], Morten M. Smedskjaer[1,a)]

1. Department of Chemistry and Bioscience, Aalborg University, Aalborg 9220, Denmark

2. Key Laboratory of Ocean Energy Utilization and Energy Conservation of Ministry of Education, Dalian University of Technology, Dalian 116024, China

3. School of Microelectronics, Northwestern Polytechnical University, Xi'an 710072, China

4. Science and Technology Division, Corning Incorporated, Corning, NY 14831, USA

5. Neutron Scattering Division, Spallation Neutron Source, Oak Ridge National Laboratory, Oak Ridge, TN 37831, USA

a)Author to whom correspondence should be addressed:

(Morten M. Smedskjaer, mos@bio.aau.dk).

Abstract

The glassy state of zeolitic imidazolate frameworks (ZIFs) has shown great potential for energy-related applications, including thermoelectrics and solid electrolytes. However, their thermal conductivity (κ), an essential parameter influencing thermal dissipation, remains largely unexplored. In this work, using a combination of experiments, atomistic simulations, and lattice dynamics calculations, we investigate κ and the underlying heat conduction mechanism in ZIF glasses with varying ratios of imidazolate (Im) to benzimidazolate (bIm) linkers. The substitution of bIm for Im tunes the node-linker couplings but exhibits only a minor impact on the average diffusivity of low-frequency lattice modes. On the other hand, the linker substitution induces significant volume expansion, which in turn suppresses the contributions from lattice vibrations to κ, leading to decreased total heat conduction. Furthermore, spatial localization of internal high-frequency linker vibrations is promoted upon the substitution, reducing their mode diffusivities. This is ascribed to structural deformations of the bIm units in the glasses. Our work unveils the detailed influences of linker substitution on dual heat conduction characteristics of ZIF glasses and guides the κ regulation of related hybrid materials in practical applications.

Keywords: Metal organic frameworks; Thermal conductivity; Linker substitution; Lattice dynamics.

I. INTRODUCTION

Metal-organic frameworks (MOFs) are hybrid materials assembled from metal nodes and organic linkers. Due to their high porosity and internal surface area, they show great potential in various applications, such as gas storage [1,2], chemical separation [3], and catalysis [4]. These applications usually involve significant heat generation and dissipation [5,6], influencing the practical performance of relevant storage or separation devices. Therefore, an essential property that needs to be well-understood is the thermal conductivity (κ), which determines the material's ability to conduct heat, and thus the inherent temperature change in the MOF device and in turn its optimal operating conditions [6]. Considering their numerous topological frameworks and tunable compositions, MOFs are also interesting objects for understanding heat transport in complex organic-inorganic (hybrid) solids [7]. Of particular interest are the respective roles of the inorganic and organic components in thermal conduction as well as the related structure-property relationships.

Considering these theoretical and practical significances, great efforts have been dedicated to clarifying the variation of κ in different MOFs and the underlying heat transfer mechanisms. Both experimental [8-12] and molecular dynamics (MD) simulations [9,13,14] have consistently identified that most MOF crystals possess extremely low κ values (typically below 1 W m^{-1} K^{-1}, e.g., 0.32 W m^{-1} K^{-1} for MOF-5 [8] and 0.69 W m^{-1} K^{-1} for HKUST-1 [9]). This limited heat conduction ability can cause a temperature rise of 100-250 K in MOF samples when they are loaded into high-pressure vessels with CH_4 or CO_2 [6], greatly increasing the risk of thermal failure. On the other hand, the low κ values make MOFs potential candidates as thermoelectric materials when combined with high electrical conductivity and thermopower [15,16]. Both aspects have promoted further research into how κ of MOFs can be adjusted. In particular, MD simulations have been used to investigate the effects of pore size, shapes [17], defects [18], functional groups [19], mechanical strain [20], and guest filler infiltration[21] on heat transport, reporting an overall decrease in κ with increasing pore size and fraction of lattice defects [17,18]. Importantly, Wieser *et al.* identified the node-linker coordination bond to be the primary bottleneck for heat conduction in MOFs [22,23]. There has also been recent interest in the heat transport of other analogous covalent-organic frameworks (COFs) [24-26] and hydrogen-bonded organic frameworks (HOFs) [27], in which κ can be tuned by varying porosity [25], pore size [24], and electrostatic

interactions [27].

Although significant progress has been made in understanding heat transport in crystalline MOFs, interest in the heat transport of the new family of glassy MOFs (accessible through melt-quenching of some MOF families [28,29]) has only recently emerged. Among them, zeolitic imidazolate framework (ZIF) glasses are particularly interesting, as they exhibit good glass-forming ability and processability, and have thus been identified as candidates for, e.g., grain-boundary-free glass membranes [30,31] and high-performance anodes [32,33] or electrolytes [34] for lithium-ion batteries. Recent experiments and MD simulations have found that glassy ZIFs exhibit *higher* κ than their crystalline counterparts [35], in contrast to the common reduction in κ upon glass formation. This was ascribed to the increase in density upon vitrification combined with longer mean free paths [36]. This higher κ of the glass phase is beneficial for promoting thermal dissipation processes, and understanding the κ of various MOF glasses is thus vital to facilitate their potential applications.

In general, disordered glass structures are known to trigger a diffusive-like heat conduction picture [37,38], distinct from the particle-like phonon transport in crystals. The inherent disorder of glass phases also invalidates traditional computational methods (e.g., Boltzmann transport equation) to estimate phonon properties. Therefore, specifically developed theories must be used to properly evaluate κ of glass materials [39,40]. That is, the employed methods and clarified principles for crystalline MOFs cannot be directly referenced in the case of glassy MOFs, sparking our interest in further investigations of their heat conduction behavior and mechanism. Unlike the long-range periodic topologies in crystalline MOFs that highly influence phonon propagation and thus κ values, κ of disordered MOF glasses is mostly dominated by their composition and interatomic interactions, as these determine vibrational characteristics and corresponding diffusive heat conduction. To this end, the compositions of MOF glasses can be modified by mixing the organic linkers [41-43], akin to their crystalline analogs. For instance, the molar ratio of the two linkers imidazolate (Im, $C_3H_3N_2^-$) and the larger benzimidazolate (bIm, $C_7H_5N_2^-$) can be tuned in a rather wide range (from 4.7:1 to 99:1) in ZIF-62 [41]. This linker substitution has been identified as an effective approach to regulate the melting behavior [41] as well as the electronic and optical properties [44] of ZIF glasses. However, the impact of such linker substitution on thermal conductivity remains unexplored.

In this work, we employ a lattice dynamics-based method along with a recently developed machine-learning (ML) potential for ZIF materials[45] to clarify the heat transport properties of ZIF glasses with varying Im/bIm linker ratios. We firstly validate this theoretical approach by comparing simulated results with experimental measurements of glass structures (using neutron scattering) and thermal conductivity (using time-domain thermoreflectance) of ZIF-62 glass. Then, by identifying the dual vibrational patterns in ZIF glasses, we discuss how linker substitution influences vibrational modes and the corresponding contributions to heat conduction. These findings provide insights into the heat transport of ZIF glasses and other similar MOF materials, ultimately guiding the design of their structures and compositions to realize preferred thermal properties for practical applications.

II. EXPERIMENTAL METHODS

A. Synthesis of ZIF glass

To prepare the ZIF-62 ($Zn(Im)_{1.75}(bIm)_{0.25}$) glass, we followed the procedure described in Ref. [35]. Briefly, crystalline ZIF-62 was first prepared using a traditional solvothermal method. Solutions of 0.6 M $Zn(NO_3)_2$, 4.0 M Im, and 0.5 M bIm in N, N-dimethylformamide (DMF) were mixed in a Zn/Im/bIm molar ratio of 1:13.5:1.5, totaling 65 mL, and further diluted with 10 mL of DMF. The solution was stirred at room temperature for 30 minutes and then heated to 403 K for 48 hours. The obtained crystals were filtered, washed with DMF and dichloromethane, and dried at 373 K. Glasses were then prepared by making a green body of crystalline ZIF-62 with a diameter of 13 mm by compressing 200 mg of crystal under a uniaxial pressure of 40 MPa. The pellet was then moved to a furnace, heated to 733 K at a rate of 10 K min^{-1} in an argon atmosphere, held isothermally for 5 minutes, and then cooled to room temperature at a rate of 10 K min^{-1}. The subsequent sample characterizations were consistent with our previous study [35].

B. Neutron scattering experiment

Time-of-flight (TOF) neutron scattering experiments were performed using the Nanoscale-Ordered Materials Diffractometer (NOMAD) at the Spallation Neutron Source (SNS) of Oak Ridge National Lab to obtain the neutron differential correlation functions $D(r)$ of synthesized ZIF-62 glass. The glass sample (~200 mg) was loaded into quartz capillaries with an inner diameter of 2.8 mm and an

outer diameter of 3 mm. The measurement was conducted for an accelerator proton charge with a measuring time of about 34 min. The collected neutron data were processed by autoNOM, a collection of Python and IDL programs specifically developed for NOMAD. A more comprehensive description of data treatment can be found in Ref. [46].

C. Thermal conductivity measurement

The non-contact time-domain thermoreflectance (TDTR) technique was employed to characterize the κ of the ZIF-62 glass sample. TDTR is a powerful and versatile pump-probe method to measure the thermal properties of various bulk materials and thin films, especially for μm-sized samples [47]. The synthesized ZIF glass with the size of about 3×3×1 mm^3 was first polished and its surface was then pre-coated with 80-nm-thick aluminum (Al) film serving as the optical transducer. During the TDTR experiment, a pump beam deposited a periodic heat flux on the Al film adjacent to the sample; a delayed probe beam was used to detect the corresponding temperature evolution of the metal film through the reflectance change (see Fig. S1a). In this work, a laser with a wavelength of 785 nm was split into a pump beam with 6 mW and a probe beam with 3 mW. The pump beam was modulated at 4.12 MHz. The reflected probe beam was converted into electrical signals by a photodiode detector. A radio frequency lock-in amplifier then outputted an in-phase (V_{in}) signal and an out-of-phase (V_{out}) signal at the modulation frequency.

When processing the TDTR data, the ratio between the in-phase and out-of-phase signals (V_{in}/V_{out}) was fitted by the heat conduction model [47] to derive the unknown thermal properties of the sample (see Fig. S1b). Note that the V_{in}/V_{out} signals have adequate sensitivity to the κ of the ZIF glass (see Fig. S2), which thus can be accurately determined. Particularly, we used the laser beam with a small spot size of r = 12 μm to obtain the intrinsic κ of the glass sample from its local regions. Using a heat diffusion model considering realistic experimental conditions [48], we estimated the local temperature rise due to the TDTR laser heating to be about 20 K. Such a temperature rise was included in the subsequent TDTR analysis and the final measurement temperature was thus 310 K. The final κ result was taken as the average from six separate measurements on different sample areas (see Table S1). The sensitivity analysis and the description of the determination of several input parameters for TDTR analysis are given in the Supplementary Material. A more detailed

introduction to the TDTR technique and data processing can be found in Ref. [47,49].

III. COMPUTATIONAL METHODS

A. Glass preparation

The atomic structure of crystalline ZIF-62 (from the work of Widmer *et al.* [50]) with the idealized composition of $Zn(Im)_{1.75}(bIm)_{0.25}$ was utilized as the starting configuration, in which Im linkers were randomly substituted by bIm, or *vice versa*, to create a series of mixed linker models ($Zn(Im)_{2-x}(bIm)_x$, x = 0-1). Note that we limited the maximum fraction of bIm linkers to 50% (x = 1.0), which has been experimentally realized in mechanically-induced amorphous ZIFs [51]. The atomic interactions for these various ZIF glass models were described by a recently developed ML force field for ZIF materials (training details and validation of this force field can be found in Ref. [45] and our data repository at https://github.com/OxideGlassGroupAAU/DeepZIF).

Based on the constructed crystalline models, ZIF glasses were then prepared using the melt-quenching process. Specifically, due to the requirement of third-order force constant data (computationally scaling $(3N)^3$, where N is the number of atoms) and a significant computational expense in the κ calculations, we employed unit cell configurations of only 272 atoms for $Zn(Im)_2$ and 368 atoms for $Zn(Im)_{1.0}(bIm)_{1.0}$. This resulted in large density fluctuations during the simulations, and we thus pre-calculated the densities of larger-size glasses by melt-quenching 3×3×3 crystalline models under the isothermal–isobaric (*NPT*) ensemble at 1 bar. These density values were then employed to scale the initial sizes of the unit cell crystalline models. Based on this, and under the canonical (*NVT*) ensemble and periodic boundary conditions, the models were firstly relaxed at 10 K for 7.5 ps and heated up to 300 K, followed by a further equilibrium for 12.5 ps. The system was subsequently heated to 1500 K, with a period of 50 ps to melt the crystals. The produced liquid was relaxed for another 50 ps and subsequently quenched to room temperature at a cooling rate of 5 K/ps, thus transforming the liquid into a glassy state. All MD simulations were carried out using the LAMMPS package [52] and a time step of 0.25 fs. The temperature was controlled by the Nosé−Hoover thermostat with a damping parameter of 25 fs, and pressure (when pre-determining the density values using the *NPT* ensemble) was controlled by the Nosé−Hoover barostat with a damping parameter of 250 fs. Finally, we used the R.I.N.G.S. package [53] to analyze

ring statistics of the simulated glasses, whose structural characteristics were further characterized by the simulated $D(r)$ and coordination numbers using the I.S.A.A.C.S. code [54].

B. Thermal conductivity calculations

The quasi-harmonic Green-Kubo (QHGK) method [39,40] based on the κALDo package [55] was employed to calculate κ of the simulated ZIF glasses with varying Im/bIm ratios. QHGK is a novel unified lattice dynamics approach to treat both crystalline and amorphous materials, giving κ as

$$\kappa_{\alpha\beta} = \frac{1}{V}\sum_{ij} c_{ij}\, v_{ij}^{\alpha}\tau_{ij}^{\circ}v_{ij}^{\beta}, \quad (1)$$

where V is the volume of the system, c_{ij}, τ_{ij}°, v_{ij} are the generalized specific heat, mode lifetime, and velocity, respectively (for detailed formula derivations please see Ref. [40]), α and β denote directions, and subscripts i and j refer to the index of the eigenvectors of the dynamical matrix. Using the last three terms in Equation (1), the mode diffusivity D_i can be expressed as

$$D_i = \sum_j v_{ij}^{\alpha}\tau_{ij}^{\circ}v_{ij}^{\beta}. \quad (2)$$

It has been verified that QHGK yields κ results in satisfactory agreement with equilibrium MD simulations under the Green-Kubo formulation (GK-EMD) [40]. In addition, compared with the GK-EMD approach, the QHGK method can be used for extracting thermal transport properties and analyzing per-mode contributions. To calculate κ of the prepared ZIF glasses, we quenched the structures to 0 K followed by an energy minimization. Then, the required second- and third-order force constants were obtained through the finite displacement method implemented in the LAMMPS package, with a displacement length of 1.0×10^{-5} Å. The subsequent QHGK calculations were performed at 300 K and considering the classic phonon populations. The final κ results were taken as the average of four replicated calculations using different quenched glass models. For comparison, we also calculated κ using the GK-EMD approach [56] (see Supplementary Material).

To test for size effects in the final estimation of κ, we prepared the $Zn(Im)_2$ glass using an extended crystalline box (2×1×1 supercell), finding a κ value close to that of the unit-cell-quenched glass ($\kappa_{unitcell}$ = 0.42 ± 0.01 W m^{-1} K^{-1}; $\kappa_{supercell}$ = 0.44 ± 0.01 W m^{-1} K^{-1}). Besides, our GK-EMD calculations based on the unit-cell and 2×2×2 supercell configurations also yielded consistent results

within error bars (see Fig. S3). This small size effect is in accordance with the previous finding that the mean free paths of ZIF glasses are below 1 nm, i.e., smaller than the typical length of our simulation boxes (~1.4 nm) [36].

C. Lattice dynamics analysis

Several lattice dynamics parameters were further evaluated to characterize the vibrational features of ZIF glasses. First, the second-order force constants were used to calculate the dynamical matrix, whose diagonalization gives the $3N$ eigenvalues ω_i^2 (i = 1, 2, …, $3N$) and corresponding normalized eigenvectors $\boldsymbol{e}_i$, where N is the number of atoms in the system. The partial vibrational density of states (VDOS) of each atomic species is then given by [57]

$$\mathrm{VDOS}(\omega)=\frac{1}{3N}\sum_{i=1}^{3N}\sum_{j=1}^{N_\alpha}\left|\boldsymbol{e}_{j,i}\right|^2\delta(\omega-\omega_i), \tag{3}$$

where N_α is the number of specific atomic species α (α = Zn, N, C, H for ZIF glasses studied here), and $\boldsymbol{e}_{j,i}$ is part of eigenvector $\boldsymbol{e}_i$ that contains the component of atom j. Adding the partial VDOS of all atomic species gives the total VDOS of the system.

The phase quotient (PQ) is another effective parameter to analyze the vibrational dynamics of amorphous materials [58]. As introduced by Allen and Feldman [38], PQ characterizes the extent to which an atom moves in the same or opposite direction relative to its nearest neighbors (for the typical phonon picture, denoted as acoustic and optical modes, respectively). Based on the calculated eigenvectors, the definition of PQ for specific atomic species α is

$$\mathrm{PQ}(\omega)=\frac{\sum_{j=1}^{N_\alpha}\boldsymbol{e}_{j,i}\cdot\boldsymbol{e}_{k,i}}{\sum_{j=1}^{N_\alpha}\left|\boldsymbol{e}_{j,i}\cdot\boldsymbol{e}_{k,i}\right|} \tag{4}$$

where $\boldsymbol{e}_{k,i}$ is the eigenvector of the nearest neighboring atom k of the atom j. Atomic species α moving in the perfect in-phase pattern with respect to its nearest neighbors yields PQ = 1, while a PQ value of -1 corresponds to every atom moving in the opposite direction of its neighbors.

Finally, the so-called participation ratio (PR) was calculated to analyze the vibrational localization effect,

$$\mathrm{PR}(\omega)=\frac{\left(\sum_{j=1}^{N}\left|\boldsymbol{u}_{j,i}\right|^{2}\right)^{2}}{N\sum_{j=1}^{N}\left|\boldsymbol{u}_{j,i}\right|^{4}}, \quad (5)$$

where $\boldsymbol{u}_{j,i}=\boldsymbol{e}_{j,i}/\sqrt{M_j}$ is the atomic amplitude and M_j is the mass of atom j. If the vibrational mode behaves as the propagative pattern in which all atoms participate equivalently, its PR value is 1. On the other hand, the PR values of the diffusive-like modes in amorphous materials usually do not exceed 0.6 [59], while localized vibrations are typically discerned as the modes with PR < 0.15.

IV. RESULTS AND DISCUSSION

A. ZIF glass structures

Before modeling the vibrations and heat conduction of the simulated ZIF glasses, we first analyze their atomic-scale structures. Fig. 1a shows the representative structural features in the simulated ZIF glasses. We find that the Zn-Zn pair exhibits a characteristic amorphous structure, differing from the original long-range-ordered crystalline framework (see Fig. S4 for snapshots of ZIF glasses with various compositions). This disorder is also evident from the radial distribution function (RDF) for the Zn-Zn atom pairs, wherein the significant peaks of the crystalline phases above 7 Å vanish and quickly approach a value of ~1 (i.e., a randomicity) upon glass formation (see Fig. S5a and S5b). In contrast, the Zn-N RDFs for both crystalline and glassy phases (Fig. S5c and S5d) are relatively similar, signifying the reconstruction of short-range Zn-N linkage networks during the melt-quenching process [60]. Consequently, apart from a small fraction of three-fold coordinated Zn (~ 6%), most Zn atoms in the glassy phases preserve four-fold coordination. This observation is in line with *ab initio* MD results [61], with the deviation from purely tetrahedral sites possibly due to the extremely high cooling rates used in the MD quenching procedure. Furthermore, based on the calculated ring statistics, the integrity of organic linkers in glassy ZIFs is preserved, as also evident from the nearly unchanged C-C RDFs (Fig. S5e and S5f).

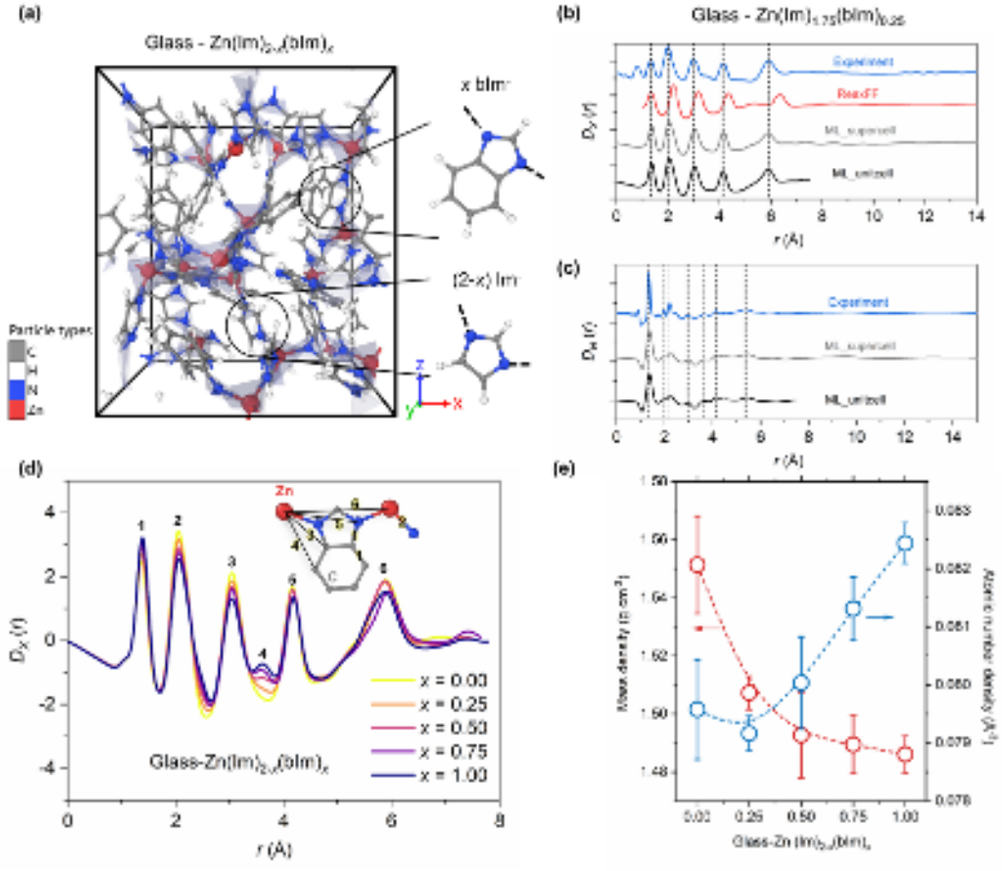

FIG. 1. (a) Representative atomic structure of simulated $Zn(Im)_{2-x}(bIm)_x$ glass, in which the Im and bIm organic linker units are highlighted. (b) Simulated X-ray $D(r)$ of $Zn(Im)_{1.75}(bIm)_{0.25}$ glass as obtained from unit cell and supercell crystalline models. Available experimental data [28] and the simulated result from the previous ReaxFF MD simulations [35] are also shown for comparison. The first peak of the experimental $D(r)$ below 1 Å was considered as an artifact according to Ref. [28]. (c) Simulated neutron $D(r)$ of $Zn(Im)_{1.75}(bIm)_{0.25}$ glass as obtained from unit cell and supercell crystalline models. The result from our neutron experiment is also shown for comparison. (d) Simulated X-ray $D(r)$ curves of ZIF glasses with varying linker components. The inset illustrates the peak assignment in the short-range node-linker structure. (e) Changes in mass density and atomic number density of the simulated ZIF glasses upon linker substitution.

Next, we validate the accuracy of the simulated glassy structures by calculating the X-ray $D(r)$ of $Zn(Im)_2$ and $Zn(Im)_{1.75}(bIm)_{0.25}$ glasses (i.e., regular ZIF-4 and ZIF-62) and compare them with both previous reactive force field (ReaxFF) MD simulations [35,62] and available experimental X-ray total scattering data [28]. As shown in Fig. S6a and Fig. 1b, the experimental X-ray $D(r)$ curves of $Zn(Im)_2$ and $Zn(Im)_{1.75}(bIm)_{0.25}$ glasses possess several distinct peaks corresponding to the short-

range-order features below 6 Å (see Fig. 1d for the detailed assignment of these sharp features to atomic pairs). These features, however, cannot be adequately reproduced by previous ReaxFF simulations, as suggested by significant peak shifts. By contrast, the ML potential utilized in this work exhibits superior performance. It reliably reproduces the experimental peak positions and intensities, albeit with slight shifts of simulated curves towards higher *r*, possibly due to density differences. It should be emphasized that X-ray $D(r)$ is more sensitive to Zn-N polyhedral [63]. Therefore, to further check our simulated structures, we also measure the neutron $D(r)$ (more sensitive to the arrangement of organic linkers) of our synthesized $Zn(Im)_{1.75}(bIm)_{0.25}$ glass sample, which we, together with previously published neutron result of $Zn(Im)_2$ glass [63], compare with our simulated neutron $D(r)$ in Fig. 1c and Fig. S6b. From this comparison we find very good consistency between experimental and simulated spectra, although some experimental peaks are sharper. This indicates that our ML-based simulations can provide reasonable descriptions of the overall structural characteristics of ZIF glasses, which is one of the key factors for accurate predictions of corresponding vibrational features and heat conduction.

We further compare the simulated X-ray $D(r)$ under different linker ratios to investigate the effects of linker substitution on the glass structures (Fig. 1d). Interestingly, despite the emergence of small peaks at ~3.6 Å with higher fractions of bIm units (the additional Zn-C pair), the total $D(r)$ curves of the various ZIF glasses exhibit similar features, with only minor differences in peak intensities. This demonstrates the similar short-range structural characteristics of the glasses, especially for the Zn-Zn and Zn-N sublattices (see Fig. S7 for corresponding partial X-ray $D(r)$ curves). Nevertheless, a significant structural expansion upon adding the larger bIm units is observed, including decreased mass density but increased atomic number density for higher bIm/Im ratio (Fig. 1e). The latter can be attributed to both volume expansion and increased atomic numbers. The calculated densities of the $Zn(Im)_2$ and $Zn(Im)_{1.75}(bIm)_{0.25}$ glasses are 1.55 g cm^{-3} and 1.51 g cm^{-3}, respectively, in good agreement with the experimental observations of 1.62 g cm^{-3} and 1.57 g cm^{-3}, respectively [28].

B. Vibrational characteristics

Based on good agreement between the simulated structures and the experimental results, we next study the vibrational characteristics of the simulated glasses by analyzing the partial vibrational

density of states (VDOS). Fig. 2a depicts the partial VDOS for the different atomic species in the representative $Zn(Im)_{1.0}(bIm)_{1.0}$ glass (see Fig. S8 for the partial VDOS of other glasses). We find that the VDOS curves of the inorganic nodes (Zn) and organic linkers (C, H, N) exhibit contrasting frequency ranges, i.e., the former has an upper boundary of approximately 10 THz, while the C, H, and N vibrations feature broad modes extending up to 100 THz. This large vibrational mismatch, arising from the mass difference between the inorganic and organic units, is an inherent feature of ZIFs (and other MOFs) and it is commonly regarded as the main origin of their extremely low κ [64].

More importantly, our VDOS calculations have revealed dual vibrational patterns of hybrid ZIF glasses that are distinct from those of conventional inorganic glasses, i.e., a band gap emerging at around 10 THz across all the simulated VDOS (see Fig. 2a and Fig. S8). Visualization of the eigenvectors allows us to pinpoint the low-frequency modes below the gap as the lattice modes contributed by the motions of all atomic species (see the example of eigenvector visualization in the inset of Fig. 2a). Each vibrational mode can be further elucidated by calculating the so-called phase quotient (PQ), which describes the in-phase acoustic-like (PQ = 1) or out-of-phase optical-like (PQ = -1) behavior of the modes. As displayed in Fig. 2b, below 10 THz, the C, H, and N atoms consistently exhibit positive PQ values close to 1, indicating that the atoms move in almost the same directions with respect to their nearest neighbors, providing nearly rigid linker units. Conversely, from 0 to 10 THz, the PQ for Zn gradually evolves from 1 to -1, signifying the transformation from the in-phase to out-of-phase patterns of Zn motions relative to their neighboring N atoms. Therefore, we note that these vibrations below ~10 THz should be treated as the lattice modes composed of the relative motions between metal nodes and rigid organic linkers. Regarding the high-frequency vibrations above the gap, the visualization of eigenvectors shows that these are internal linker modes composed of only the C, H, and N motions (see the inset of Fig. 2a). This can be further clarified from the fluctuation of PQ values between -1 and 1 for C, H, and N atoms at frequencies above 10 THz (Fig. 2b). Within these vibrational patterns, the relative in-phase and out-of-phase motions of the constituent atoms enable the significant flexibility of the organic linkers.

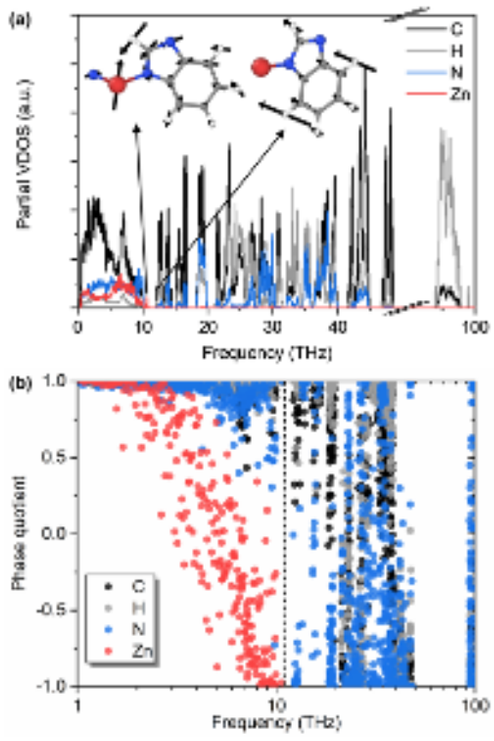

FIG. 2. (a) Partial VDOS curves of different atomic species in the representative simulated $Zn(Im)_{1.0}(bIm)_{1.0}$ glass. The insets represent the visualizations of node-linker vibrations to distinguish lattice and linker modes (see the main text for the clarification of these two mode patterns), wherein the black arrows denote the normal mode displacement vectors. (b) Mode phase quotient parameters of different atomic species in the representative simulated $Zn(Im)_{1.0}(bIm)_{1.0}$ glass as a function of frequency.

C. Thermal conductivity

In the following, we study the heat transfer properties of the ZIF glasses. First, based on the simulated structures, the κ values at 300 K are determined using the QHGK method (see black symbols in Fig. 3a). For typical $Zn(Im)_2$ and $Zn(Im)_{1.75}(bIm)_{0.25}$ glasses, the simulated κ values are 0.42±0.01 W m^{-1} K^{-1} and 0.39±0.01 W m^{-1} K^{-1}, respectively, deviating from the previous results based on ReaxFF MD simulations (0.72 W m^{-1} K^{-1} for $Zn(Im)_2$ glass and 0.95 W m^{-1} K^{-1} for $Zn(Im)_{1.75}(bIm)_{0.25}$ glass) [35]. This discrepancy may be ascribed to the different simulated structural characteristics using the ReaxFF force field [65]. To verify the accuracy of our κ calculations, we experimentally synthesized the bulk $Zn(Im)_{1.75}(bIm)_{0.25}$ glass (for other compositions, e.g., $Zn(Im)_2$ glass, it tends to foam strongly during melting, thus hindering the formation of large bulk samples). We then measured its κ using the non-contact time-domain thermoreflectance (TDTR) technique,

which has the advantage of focusing on local dense sample areas to extract intrinsic thermal properties [47]. The derived κ from six separated measurements on different sample regions is found to be 0.33±0.04 W m^{-1} K^{-1}, in good agreement with our simulated result of 0.39±0.01 W m^{-1} K^{-1}. In contrast, the previously reported experimental values are somewhat lower (0.12 W m^{-1} K^{-1} for $Zn(Im)_2$ glass and 0.13 W m^{-1} K^{-1} for $Zn(Im)_{1.75}(bIm)_{0.25}$ glass), which could be ascribed to the difference in the characterization method (laser flash analysis of powder pellet samples [35]). The porous micro-structures can lead to large thermal contact resistance between grains and consequently a lower value of κ compared to that of the bulk structure. Such a challenge in accurately characterizing the physical properties of MOF materials with small grain sizes has been widely discussed [10,66]. In this regard, the present theoretical calculations with the ML force field can not only accurately simulate the ZIF glass structures, but also well describe the interatomic interactions, thus offering an effective strategy to compute the intrinsic κ values of ZIF glasses.

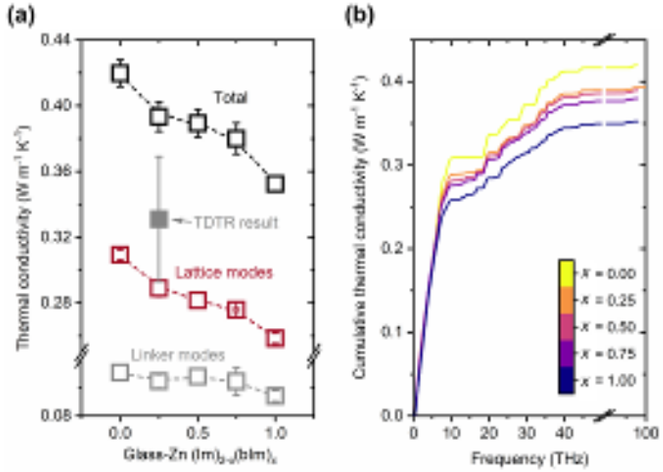

FIG. 3. (a) Total thermal conductivity and partial contributions from lattice modes and linker modes as a function of the fraction of bIm linkers in the simulated ZIF glasses. The experimental thermal conductivity value of the $Zn(Im)_{1.75}(bIm)_{0.25}$ glass from the present TDTR measurements is also shown for comparison. (b) Cumulative thermal conductivity for the different simulated ZIF glasses as a function of the vibrational frequency.

Comparing the ZIF glasses with varying bIm/Im ratios, the QHGK calculations predict a decrease in κ with an increasing fraction of bIm linkers, from 0.42 W m^{-1} K^{-1} for $Zn(Im)_2$ glass to 0.35 W m^{-1} K^{-1} for $Zn(Im)_{1.0}(bIm)_{1.0}$ glass. This change can be reproduced by GK-EMD calculations (see Fig.

S3) and should not be solely attributed to the decreased mass density, considering both the varying volumes and compositions of the studied glasses. Note that we have distinguished the dominant coherence components [67] (off-diagonal terms [39], see Supplementary Material) of heat transport in the various ZIF glasses and found that they feature an approximate constant contribution of ~85% (see Fig. S9). We have also checked the dependence of κ on atomic coordination, another key parameter that possibly influences the heat conduction of amorphous materials [68], but found no evident correlation between κ and the average Zn-N coordination numbers (see Fig. S10). Therefore, we attempt to elucidate the origin of the decrease in κ based on the identified dual vibrational characteristics. In detail, based on the per-mode κ information of the QHGK method, the total κ values can be decomposed into two parts, i.e., κ_{lattice} and κ_{linker}, by summarizing the partial contributions of each lattice and liker modes, respectively (Fig. 3a). This decomposition shows the limited heat conduction abilities of numerous high-frequency linker modes, as also reasoned by the sluggish increase of mode-cumulative κ above 10 THz (Fig. 3b). Furthermore, their contributions remain almost constant for various linker ratios (Fig. 3a). In contrast, the lattice modes of ZIF glasses account for more than half of the total κ. This main contribution is manifested as the rapid increase of the mode-cumulative κ in the low-frequency range (Fig. 3b). However, κ_{lattice} decreases as the structures incorporate more bIm linkers (Fig. 3a), i.e., the decrease in κ_{lattice} governs the observed reduction in κ of the ZIF glasses with increasing bIm/Im ratio.

D. Thermal diffusivity

To understand the changes in lattice and linker contributions to the total κ, we analyze the per-mode diffusivity D_i, which quantitatively describes the energy-carrying capability of each vibrational mode. Fig. 4 shows the spectra of mode D_i for ZIF glasses with different linker constituents. Specifically, the D_i values of low-frequency lattice modes exhibit a complex evolving trend. That is, increasing the fraction of bIm linkers leads to a "sharper" shoulder with the higher peak value at around 6 THz, but noticeably reduced D_i for the modes below 2 THz. Here, it is worth emphasizing that the QHGK method shares a similar conceptual basis with the well-known Allen-Feldmann theory [37,38], where thermal diffusion is accomplished by mode correlation. Therefore, the observed

variations in lattice D_i upon linker substitution represent the evolution of mode couplings, which can be further elucidated by investigating the low-frequency partial VDOS. In particular, the vibrational match between Zn and N atoms should be highlighted as it controls the thermal transport between inorganic and organic parts, namely, lattice contributions.

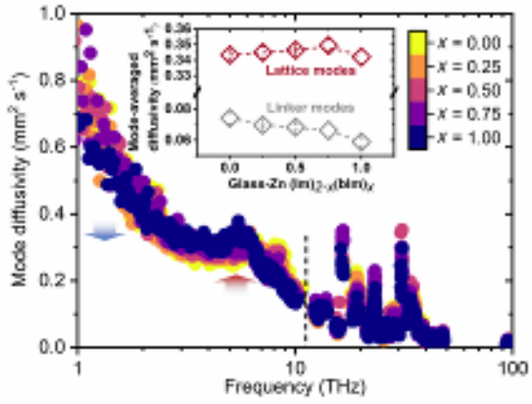

FIG. 4. Spectra of mode diffusivity of ZIF glasses with varying linker components. The red and blue arrows mark the regions of increased and decreased mode diffusivities with higher fractions of bIm linkers. The inset shows the changes in mode-average diffusivities of lattice and linker modes.

From partial VDOS results, we find that the prominent peaks of Zn-VDOS at around 7.5 THz and 9 THz in the $Zn(Im)_2$ glass (red curve in Fig. 5a) experience significant shifts towards lower frequencies upon bIm linker substitution, ultimately manifesting as a strong peak at ~6.5 THz in the $Zn(Im)_{1.0}(bIm)_{1.0}$ glass (Fig. 5b). Alongside the changes of Zn-VDOS, the strong peak of N-VDOS at ~6 THz in the $Zn(Im)_2$ glass (blue curve in Fig. 5a) diminishes and transforms into a more uniformly distributed pattern across a wide frequency range in the $Zn(Im)_{1.0}(bIm)_{1.0}$ glass (Fig. 5b). Consequently, there is an intensified Zn-N vibrational match in the intermediate frequency range of 4-8 THz for the high-linker-ratio glass, characterized by reduced intensity difference between Zn-VDOS and N-VDOS (see Fig. 5b). This enhanced match facilitates thermal diffusion between Zn nodes and N atoms through stronger vibrational coupling [69], in accordance with the "sharper" shoulder of the lattice D_i (Fig. 4). Furthermore, we observe decreased intensities of both Zn and N VDOS below 2 THz, which are possibly the origins of the lower D_i in the same frequency range. Surprisingly, despite these changes of spectral D_i and related vibrational couplings for lattice modes, their mode-averaged D displays relatively minor fluctuations (see the inset of Fig. 4). This is a

consequence of the levelling effect caused by both increasing and decreasing D_i in the different frequency ranges.

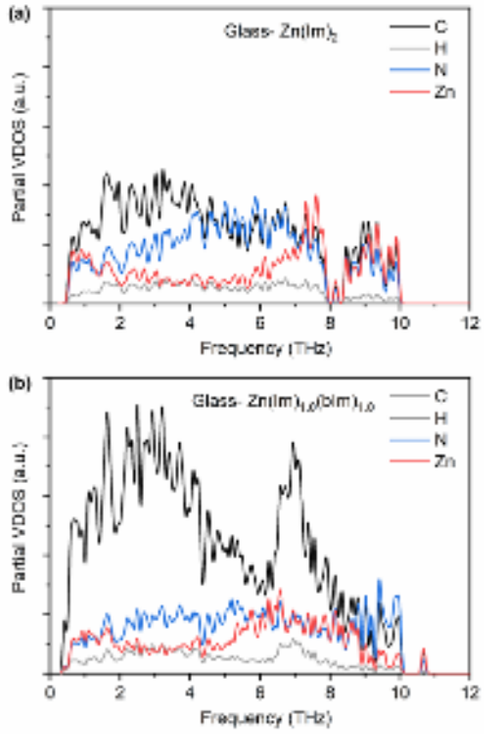

FIG. 5. Low-frequency partial VDOS for different atomic species in the simulated (a) $Zn(Im)_2$ and (b) $Zn(Im)_{1.0}(bIm)_{1.0}$ glasses. The red and blue curves represent the VDOS of zinc and nitrogen atoms, respectively, whose couplings highly influence the thermal diffusion in the ZIF glasses. The black and grey curves represent the VDOS of the carbon and hydrogen atoms, respectively, in the organic linkers. Note that the enhanced intensity and additional peak at around 7 THz of carbon atoms in the $Zn(Im)_{1.0}(bIm)_{1.0}$ glass are due to additional bIm units.

Regarding the linker modes, we have observed reductions in mode D_i (see Fig. 4; Fig. S11 shows the corresponding distribution histogram) and mode-averaged D (see the inset of Fig. 4) with increasing bIm/Im ratio. Nevertheless, there are numerous peaks for the high-frequency linker modes in partial VDOS curves (see Fig. 2a and Fig. S8), making it difficult to identify mode coupling. As an alternative, we study the linker vibrations *via* the participation ratio (PR), an important parameter for characterizing the spatial localization of vibrational modes in amorphous materials. Interestingly, a positive correlation between mode D_i and PR is found for the present ZIF glasses (see Fig. S12). This observation agrees with the well-established principle that spatially

extended modes (large PR values) tend to have high thermal diffusivity [70]. As shown in Fig. 6a, the high-frequency linker modes possess significantly lower PR values compared with most lattice modes. The latter entails the collective motions of both metal nodes and organic linkers, thus easily spanning the entire hybrid lattice (see examples of mode visualizations in Fig. S13). In contrast, the linker modes are spatially confined within the organic units, accounting for their lower mode D_i (Fig. 4). More importantly, we find a pronounced effect of linker substitution, as observed from the suppression of the PR values of linker modes (see Fig. 6a for decreased PR values above 10 THz, and Fig. S14 for the corresponding distribution histogram). We consider the mode at around 28 THz as an example, which represents the motions of multiple linker units distributed in the wide space of the $Zn(Im)_2$ glass (Fig. 6b) and has a PR value of around 0.25. However, in the $Zn(Im)_{1.0}(bIm)_{1.0}$ glass with bIm linkers, the mode PR diminishes to 0.1, aligning with the vibration being spatially confined to a more localized region (Fig. 6c). The contrasting PRs indicate more severe localization of linker vibrations upon increasing bIm/Im ratio, which is the origin of the decrease in thermal diffusivity (Fig. 4).

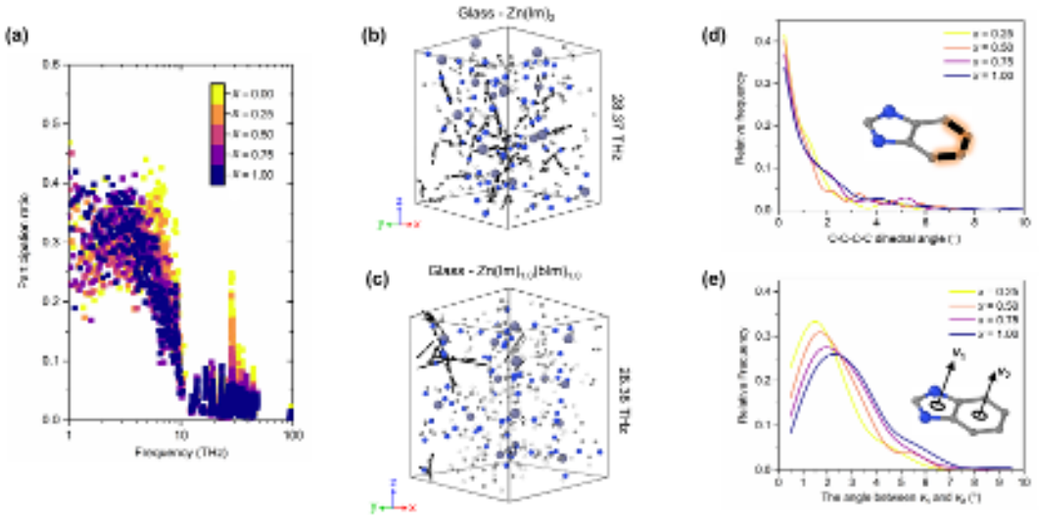

FIG. 6. (a) Mode participation ratio (PR) of the simulated ZIF glasses with different linker components. (b-c) Visualization of spatially localized linker modes at around 28 THz in simulated (b) $Zn(Im)_2$ and (c) $Zn(Im)_{1.0}(bIm)_{1.0}$ glasses. The black arrows denote the normal mode displacement vectors of atoms. (d) Distribution of C-C-C-C dihedral angle of bIm units in various ZIF glasses. (e) Distribution of the angle between the normal vectors of the 5- and 6-ring sections of bIm in various ZIF glasses.

The strong mode localization in glass materials is known to be highly correlated with their inherent structural disorder [71]. This motivates further investigations into the structural features of the organic linkers beyond those intuitively reflected by the $D(r)$. Specifically, in contrast to the planar Im rings in the $Zn(Im)_2$ glass, both the Im rings and six-membered benzene rings (in bIm) within the substituted glasses exhibit deviations from perfect planarity, as seen from the non-zero values of the N-C-C-N (Fig. S15) and C-C-C-C dihedral angles (Fig. 6d). Intriguingly, by further analyzing the distributions of these angles, we observe more pronounced ring deformations in glasses with more bIm units. Furthermore, we also compute the normal vectors of both the 5- and 6-membered rings in bIm. The increase in the angle between them with increasing bIm/Im ratio (Fig. 6e) validates the greater distortions of the individual bIm units. In other words, these results suggest that by adding more bulky ligands (bIm), additional structural disorder is introduced in the ZIF structure. This disorder consequently enhances the spatial localization of linker modes and leads to their low thermal diffusivities.

E. Heat conduction mechanisms

Finally, we discuss the detailed heat conduction mechanism, considering the lattice and linker contributions. To this end, we consider the microscopic definition of κ for glass materials, $\kappa = \Sigma c_i D_i$, where c_i is the volumetric heat capacity of mode i (simplified as k_B/V in the classical limit where k_B is the Boltzmann constant and V is the volume), and D_i is the mode diffusivity, with the summation encompassing all modes. This suggests that the heat conduction in ZIF glasses is determined by mode number (equal to $3N$ where N is the atomic number), volume, and mode diffusivity. Specifically, the extended nature of lattice modes across large lattice space (Fig. S13) enables their relatively high D_i and consequently a predominant contribution to the total κ (Fig. 3a). Moreover, the thermal diffusion through lattice vibrations is highly controlled by the mode couplings, suggesting the possibility of regulating κ by tuning the composition and thus the lattice dynamics. Indeed, we have here found that replacing Im with bIm modifies the node-linker couplings (Fig. 5) and spectral lattice D_i. Nevertheless, due to the non-monotonic changes of lattice D_i over the wide frequency ranges (Fig. 4), the corresponding mode-average D remains nearly unchanged.

Additionally, through mode recognition, we find only a slight increase in the lattice mode number with increasing bIm/Im ratio (see Fig. S16). Thus, the reduced $\kappa_{lattice}$ should be primarily ascribed to the decreased c_i, in turn resulting from the considerable volume expansion. To further confirm this, we have calculated the Bridgman parameter $g = (d\ln\kappa/d\ln V)$, which provides a convenient way to check the volume dependence of heat transport. The calculated g value of the present ZIF glasses is about 3.8, which is indeed similar to the values of other glassy systems (e.g., 3.7 for glassy atactic polypropylene [72] and 2.8 for glassy polyvinyl acetate [73]).

Concerning the linker modes, these internal motions possess low D_i values as they are restricted in localized lattice space (Figs. 6b and 6c). Moreover, the remarkable deformations of linker units (Figs. 6d and 6e) trigger even more severe vibrational localization and diminished D_i (Fig. 4). Nevertheless, the additional number of internal vibrations stemming from incorporated bIm should not be ignored. The significantly increased linker mode number (Fig. S16) with a higher bIm/Im ratio compensates for the suppressed values of D_i and c_i and leads to the approximately constant linker contribution (κ_{linker}) to total κ.

V. CONCLUSIONS

We have used a recently developed ML potential to theoretically investigate the effect of organic linker substitution in ZIF glasses on their lattice dynamics and heat conduction. The accuracy of these calculations has been confirmed by experimental validation of glass structures through neutron scattering and κ value through TDTR. Vibrational analysis and decomposition of the contributions to κ show that the incorporation of larger bIm linkers suppresses κ of ZIF glasses by reducing the contributions from lattice modes, while maintaining almost constant contributions from high-frequency linker modes. We mainly attribute the decreased lattice contributions with increasing bIm/Im ratio to the volume expansion. The almost unaffected contribution from the linkers, however, is due to both decreased mode diffusivities and increased mode numbers. More significantly, we highlight the essential role of node-linker vibrational couplings in the thermal diffusion of lattice modes. To this end, tailoring the composition to achieve relatively strong node-linker bonds or small

mass differences between building blocks can enhance mode couplings and thus heat conduction of MOF glasses. Finally, our calculations show reduced thermal diffusion from internal linker vibrations with increasing bIm/Im ratio, which is due to severe localization effects induced by deformations of the larger bIm units. This highlights the important role of structural disorder in minimizing κ. Our findings provide valuable insights into the heat conduction mechanisms of ZIFs and other MOF materials and may guide their design toward tailored κ values for relevant thermal dissipation or thermoelectric applications.

SUPPLEMENTARY MATERIAL

Supplementary Figures for this article can be found in the Supplementary Material.

ACKNOWLEDGMENTS

C.Y. gratefully acknowledges the financial support from the China Scholarship Council (Grant No. 202206060064). A portion of this research used resources at the Spallation Neutron Source, a DOE Office of Science User Facility operated by the Oak Ridge National Laboratory. Computational resources were provided by CLAAUDIA at Aalborg University.

AUTHOR DECLARATIONS

Conflict of Interest

The authors have no conflicts to disclose.

Author Contributions

Chengyang Yuan: Conceptualization (equal); Formal analysis (lead); Methodology (equal); Data curation (lead); Writing – original draft (lead). **Søren S. Sørensen**: Conceptualization (equal); Methodology (equal); Writing – review & editing (equal). **Tao Du**: Methodology (supporting); Writing – review & editing (equal). **Zhongyin Zhang**: Methodology (supporting). **Yongchen Song**: Writing – review & editing (supporting). **Ying Shi**: Methodology (supporting). **Jörg Neuefeind**:

Methodology (supporting). **Morten M. Smedskjaer**: Supervision (lead); Conceptualization (equal); Writing – review & editing (lead).

Data availability

The data that support the findings of this study are available from the corresponding author upon reasonable request.

References

[1]N. L. Rosi, J. Eckert, M. Eddaoudi, D. T. Vodak, J. Kim, M. O'Keeffe, and O. M. Yaghi, "Hydrogen storage in microporous metal-organic frameworks," Science **300**, 1127 (2003).

[2]Y. He, W. Zhou, G. Qian, and B. Chen, "Methane storage in metal-organic frameworks," Chem. Soc. Rev. **43**, 5657 (2014).

[3]S. Qiu, M. Xue, and G. Zhu, "Metal-organic framework membranes: From synthesis to separation application," Chem. Soc. Rev. **43**, 6116 (2014).

[4]J. Lee, O. K. Farha, J. Roberts, K. A. Scheidt, S. T. Nguyen, and J. T. Hupp, "Metal-organic framework materials as catalysts," Chem. Soc. Rev. **38**, 1450 (2009).

[5]J. A. Mason, J. Oktawiec, M. K. Taylor, M. R. Hudson, J. Rodriguez, J. E. Bachman, M. I. Gonzalez, A. Cervellino, A. Guagliardi, C. M. Brown, P. L. Llewellyn, N. Masciocchi, and J. R. Long, "Methane storage in flexible metal-organic frameworks with intrinsic thermal management," Nature **527**, 357 (2015).

[6]J. Wieme, S. Vandenbrande, A. Lamaire, V. Kapil, L. Vanduyfhuys, and V. Van Speybroeck, "Thermal engineering of metal-organic frameworks for adsorption applications: A molecular simulation perspective," ACS Appl. Mater. Interfaces. **11**, 38697 (2019).

[7]X. Qian, X. Gu, and R. Yang, "Thermal conductivity modeling of hybrid organic-inorganic crystals and superlattices," Nano Energy **41**, 394 (2017).

[8]B. Huang, Z. Ni, A. Millward, A. McGaughey, C. Uher, M. Kaviany, and O. Yaghi, "Thermal conductivity of a metal-organic framework (MOF-5): Part II. Measurement," Int. J. Heat Mass Transf. **50**, 405 (2007).

[9]H. Babaei, M. E. DeCoster, M. Jeong, Z. M. Hassan, T. Islamoglu, H. Baumgart, A. J. McGaughey, E. Redel, O. K. Farha, and P. E. Hopkins, "Observation of reduced thermal conductivity in a metal-organic framework due to the presence of adsorbates," Nat. Comm. **11**, 4010 (2020).

[10]J. Huang, X. Xia, X. Hu, S. Li, and K. Liu, "A general method for measuring the thermal conductivity of MOF crystals," Int. J. Heat Mass Transf. **138**, 11 (2019).

[11]J. Chae, S. An, G. Ramer, V. Stavila, G. Holland, Y. Yoon, A. A. Talin, M. Allendorf, V. A. Aksyuk, and A. Centrone, "Nanophotonic atomic force microscope transducers enable chemical composition and thermal conductivity measurements at the nanoscale," Nano Lett. **17**, 5587 (2017).

[12]B. Cui, C. O. Audu, Y. Liao, S. T. Nguyen, O. K. Farha, J. T. Hupp, and M. Grayson, "Thermal conductivity of ZIF-8 thin-film under ambient gas pressure," ACS Appl. Mater. Interfaces. **9**, 28139 (2017).

[13]B. Huang, A. McGaughey, and M. Kaviany, "Thermal conductivity of metal-organic framework 5 (MOF-5): Part I. Molecular dynamics simulations," Int. J. Heat Mass Transf. **50**, 393 (2007).

[14]R. Cheng, W. Li, W. Wei, J. Huang, and S. Li, "Molecular insights into the correlation between microstructure and thermal conductivity of zeolitic imidazolate frameworks," ACS Appl. Mater. Interfaces. **13**, 14141 (2021).

[15]L. Sun, B. Liao, D. Sheberla, D. Kraemer, J. Zhou, E. A. Stach, D. Zakharov, V. Stavila, A. A. Talin, and Y. Ge, "A microporous and naturally nanostructured thermoelectric metal-organic framework with ultralow thermal conductivity," Joule **1**, 168 (2017).

[16]K. J. Erickson, F. Léonard, V. Stavila, M. E. Foster, C. D. Spataru, R. E. Jones, B. M. Foley, P. E. Hopkins, M. D. Allendorf, and A. A. Talin, "Thin film thermoelectric metal-organic framework with high seebeck coefficient and low thermal conductivity," Adv. Mater. **27**, 3453 (2015).

[17]H. Babaei, A. J. McGaughey, and C. E. Wilmer, "Effect of pore size and shape on the thermal conductivity of metal-organic frameworks," Chem. Sci. **8**, 583 (2017).

[18]M. Islamov, H. Babaei, and C. E. Wilmer, "Influence of missing linker defects on the thermal conductivity of metal-organic framework HKUST-1," ACS Appl. Mater. Interfaces. **12**, 56172 (2020).

[19]P. Ying, J. Zhang, X. Zhang, and Z. Zhong, "Impacts of functional group substitution and pressure on the thermal conductivity of ZIF-8," J. Phys. Chem. C **124**, 6274 (2020).

[20]H. Fan, P. Ying, Z. Fan, Y. Chen, Z. Li, and Y. Zhou, "Anomalous strain-dependent thermal conductivity in the metal-organic framework HKUST-1," Phys. Rev. B **109**, 045424 (2024).

[21]H. Fan, C. Yang, and Y. Zhou, "Ultralong mean free path phonons in HKUST-1 and their scattering by water adsorbates," Phys. Rev. B **106**, 085417 (2022).

[22]S. Wieser, T. Kamencek, R. Schmid, N. Bedoya-Martínez, and E. Zojer, "Exploring the impact of the linker length on heat transport in metal-organic frameworks," Nanomaterials **12**, 2142 (2022).

[23]S. Wieser, T. Kamencek, J. P. Dürholt, R. Schmid, N. Bedoya-Martínez, and E. Zojer, "Identifying the bottleneck for heat transport in metal-organic frameworks," Adv. Theory Simul. **4**, 2000211 (2021).

[24]M. A. Rahman, C. J. Dionne, and A. Giri, "Pore size dictates anisotropic thermal conductivity of two-dimensional covalent organic frameworks with adsorbed gases," ACS Appl. Mater. Interfaces. **14**, 21687 (2022).

[25]M. A. Rahman, S. Thakur, P. E. Hopkins, and A. Giri, "Engineering the electronic and thermal properties of two-dimensional covalent organic frameworks," J. Phys. Chem. C **127**, 11157 (2023).

[26]J. Kwon, H. Ma, A. Giri, P. E. Hopkins, N. B. Shustova, and Z. Tian, "Thermal conductivity of covalent-organic frameworks," ACS Nano **17**, 15222 (2023).

[27]R. Hu, H. Fan, Y. Zhou, K. Tao, Z. Tian, and H. Ma, "Electrostatic interactions dominate thermal conductivity and anisotropy in three-dimensional hydrogen-bonded organic frameworks," Int. J. Heat Mass Transf. **221**, 125071 (2024).

[28]T. D. Bennett, Y. Yue, P. Li, A. Qiao, H. Tao, N. G. Greaves, T. Richards, G. I. Lampronti, S. A. Redfern, F. Blanc, O. K. Farha, J. T. Hupp, A. K. Cheetham, and D. A. Keen, "Melt-quenched glasses of metal-organic frameworks," J. Am. Chem. Soc. **138**, 3484 (2016).

[29]A. Qiao, T. D. Bennett, H. Tao, A. Krajnc, G. Mali, C. M. Doherty, A. W. Thornton, J. C. Mauro, G. N. Greaves, and Y. Yue, "A metal-organic framework with ultrahigh glass-forming ability," Sci. Adv. **4**, eaao6827 (2018).

[30]Y. Wang, H. Jin, Q. Ma, K. Mo, H. Mao, A. Feldhoff, X. Cao, Y. Li, F. Pan, and Z. Jiang, "A MOF glass membrane for gas separation," Angew. Chem. Int. Ed. **132**, 4395 (2020).

[31]Z. Yang, Y. Belmabkhout, L. N. McHugh, D. Ao, Y. Sun, S. Li, Z. Qiao, T. D. Bennett, M. D. Guiver,

and C. Zhong, "ZIF-62 glass foam self-supported membranes to address CH_4/N_2 separations," Nat. Mater. **22**, 888 (2023).

[32]C. Gao, Z. Jiang, S. Qi, P. Wang, L. R. Jensen, M. Johansen, C. K. Christensen, Y. Zhang, D. B. Ravnsbæk, and Y. Yue, "Metal-organic framework glass anode with an exceptional cycling-induced capacity enhancement for lithium-ion batteries," Adv. Mater. **34**, 2110048 (2022).

[33]J. Yan, C. Gao, S. Qi, Z. Jiang, L. R. Jensen, H. Zhan, Y. Zhang, and Y. Yue, "Encapsulation of nano-Si into MOF glass to enhance lithium-ion battery anode performances," Nano Energy **103**, 107779 (2022).

[34]G. Jiang, C. Qu, F. Xu, E. Zhang, Q. Lu, X. Cai, S. Hausdorf, H. Wang, and S. Kaskel, "Glassy metal–organic-framework-based quasi-solid-state electrolyte for high-performance lithium-metal batteries," Adv. Funct. Mater. **31**, 2104300 (2021).

[35]S. S. Sørensen, M. B. Østergaard, M. Stepniewska, H. Johra, Y. Yue, and M. M. Smedskjaer, "Metal-organic framework glasses possess higher thermal conductivity than their crystalline counterparts," ACS Appl. Mater. Interfaces. **12**, 18893 (2020).

[36]Y. Zhou, B. Huang, and B.-Y. Cao, "Vibrational modes with long mean free path and large volumetric heat capacity drive higher thermal conductivity in amorphous zeolitic imidazolate framework-4," Mater. Today Phys. **21**, 100516 (2021).

[37]P. B. Allen and J. L. Feldman, "Thermal conductivity of glasses: Theory and application to amorphous Si," Phys. Rev. Lett. **62**, 645 (1989).

[38]P. B. Allen, J. L. Feldman, J. Fabian, and F. Wooten, "Diffusons, locons and propagons: Character of atomic vibrations in amorphous Si," Philos. Mag. B **79**, 1715 (1999).

[39]M. Simoncelli, N. Marzari, and F. Mauri, "Unified theory of thermal transport in crystals and glasses," Nat. Phys. **15**, 809 (2019).

[40]L. Isaeva, G. Barbalinardo, D. Donadio, and S. Baroni, "Modeling heat transport in crystals and glasses from a unified lattice-dynamical approach," Nat. Comm. **10**, 3853 (2019).

[41]L. Frentzel-Beyme, M. Kloß, P. Kolodzeiski, R. Pallach, and S. Henke, "Meltable mixed-linker zeolitic imidazolate frameworks and their microporous glasses: From melting point engineering to selective hydrocarbon sorption," J. Am. Chem. Soc. **141**, 12362 (2019).

[42]M. F. Thorne, M. L. R. Gómez, A. M. Bumstead, S. Li, and T. D. Bennett, "Mechanochemical synthesis of mixed metal, mixed linker, glass-forming metal-organic frameworks," Green Chem. **22**, 2505 (2020).

[43]J. Hou, M. L. Rios Gomez, A. Krajnc, A. McCaul, S. Li, A. M. Bumstead, A. F. Sapnik, Z. Deng, R. Lin, and P. A. Chater, "Halogenated metal-organic framework glasses and liquids," J. Am. Chem. Soc. **142**, 3880 (2020).

[44]M. Xiong, X. Zhao, G. Yin, W.-Y. Ching, and N. Li, "Unraveling the effects of linker substitution on structural, electronic and optical properties of amorphous zeolitic imidazolate frameworks-62 (a-ZIF-62) glasses: A dft study," RSC Adv. **10**, 14013 (2020).

[45]T. Du, S. Li, S. Ganisetti, M. Bauchy, Y. Yue, and M. M. Smedskjaer, "Deciphering the controlling factors for phase transitions in zeolitic imidazolate frameworks," Natl. Sci. Rev., nwae023 (2024).

[46]J. Neuefeind, M. Feygenson, J. Carruth, R. Hoffmann, and K. K. Chipley, "The nanoscale ordered materials diffractometer nomad at the spallation neutron source SNS," Nucl. Inst. Methods Phys. Res. B **287**, 68 (2012).

[47]P. Jiang, X. Qian, and R. Yang, "Tutorial: Time-domain thermoreflectance (TDTR) for thermal property characterization of bulk and thin film materials," J. Appl. Phys. **124**, 161103 (2018).

[48]J. L. Braun, C. J. Szwejkowski, A. Giri, and P. E. Hopkins, "On the steady-state temperature rise during laser heating of multilayer thin films in optical pump–probe techniques," J. Heat Transf. **140**, 052801

(2018).

[49]C. Yuan, Z. Zhang, J. Zhu, J. Zhao, L. Zhang, L. Yang, Y. Song, and D. Tang, "Heat transport in clathrate hydrates controlled by guest frequency and host-guest interaction," J. Phys. Chem. Lett. **14**, 7766 (2023).

[50]R. N. Widmer, G. I. Lampronti, S. Anzellini, R. Gaillac, S. Farsang, C. Zhou, A. M. Belenguer, C. W. Wilson, H. Palmer, and A. K. Kleppe, "Pressure promoted low-temperature melting of metal-organic frameworks," Nat. Mater. **18**, 370 (2019).

[51]M. F. Thorne, A. F. Sapnik, L. N. McHugh, A. M. Bumstead, C. Castillo-Blas, D. S. Keeble, M. D. Lopez, P. A. Chater, D. A. Keen, and T. D. Bennett, "Glassy behaviour of mechanically amorphised ZIF-62 isomorphs," Chem. Commun. **57**, 9272 (2021).

[52]A. P. Thompson, H. M. Aktulga, R. Berger, D. S. Bolintineanu, W. M. Brown, P. S. Crozier, P. J. in't Veld, A. Kohlmeyer, S. G. Moore, and T. D. Nguyen, "Lammps-a flexible simulation tool for particle-based materials modeling at the atomic, meso, and continuum scales," Comput. Phys. Commun. **271**, 108171 (2022).

[53]S. Le Roux and P. Jund, "Ring statistics analysis of topological networks: New approach and application to amorphous GeS_2 and SiO_2 systems," Comput. Mater. Sci. **49**, 70 (2010).

[54]S. Le Roux and V. Petkov, "ISAACS-interactive structure analysis of amorphous and crystalline systems," J. Appl. Crystallogr. **43**, 181 (2010).

[55]G. Barbalinardo, Z. Chen, N. W. Lundgren, and D. Donadio, "Efficient anharmonic lattice dynamics calculations of thermal transport in crystalline and disordered solids," J. Appl. Phys. **128**, 135104 (2020).

[56]R. Kubo, "Statistical-mechanical theory of irreversible processes. I. General theory and simple applications to magnetic and conduction problems," J. Phys. Soc. Japan. **12**, 570 (1957).

[57]L. Pedesseau, S. Ispas, and W. Kob, "First-principles study of a sodium borosilicate glass-former. II. The glass state," Phys. Rev. B **91**, 134202 (2015).

[58]H. R. Seyf, W. Lv, A. Rohskopf, and A. Henry, "The importance of phonons with negative phase quotient in disordered solids," Sci. Rep. **8**, 2627 (2018).

[59]B. B. Laird and H. Schober, "Localized low-frequency vibrational modes in a simple model glass," Phys. Rev. Lett. **66**, 636 (1991).

[60]R. Gaillac, P. Pullumbi, K. A. Beyer, K. W. Chapman, D. A. Keen, T. D. Bennett, and F.-X. Coudert, "Liquid metal-organic frameworks," Nat. Mater. **16**, 1149 (2017).

[61]R. Gaillac, P. Pullumbi, T. D. Bennett, and F.-X. Coudert, "Structure of metal-organic framework glasses by ab initio molecular dynamics," Chem. Mater. **32**, 8004 (2020).

[62]Y. Yang, Y. K. Shin, S. Li, T. D. Bennett, A. C. Van Duin, and J. C. Mauro, "Enabling computational design of ZIFs using ReaxFF," J. Phys. Chem. B **122**, 9616 (2018).

[63]D. Keen and T. Bennett, "Structural investigations of amorphous metal-organic frameworks formed via different routes," Phys. Chem. Chem. Phys. **20**, 7857 (2018).

[64]X. Zhang and J. Jiang, "Thermal conductivity of zeolitic imidazolate framework-8: A molecular simulation study," J. Phys. Chem. C **117**, 18441 (2013).

[65]N. Castel and F.-X. Coudert, "Challenges in molecular dynamics of amorphous ZIFs using reactive force fields," J. Phys. Chem. C **126**, 19532 (2022).

[66]M. Islamov, H. Babaei, R. Anderson, K. B. Sezginel, J. R. Long, A. J. McGaughey, D. A. Gomez-Gualdron, and C. E. Wilmer, "High-throughput screening of hypothetical metal-organic frameworks for thermal conductivity," Npj Comput. Mater. **9**, 11 (2023).

[67]X. Xiang, S. Patinet, S. Volz, and Y. Zhou, "Quasilocalized vibrational modes as efficient heat carriers in glasses," Int. J. Heat Mass Transf. **210**, 124150 (2023).

[68]A. Giri, C. J. Dionne, and P. E. Hopkins, "Atomic coordination dictates vibrational characteristics and thermal conductivity in amorphous carbon," Npj Comput. Mater. **8**, 55 (2022).
[69]W.-L. Ong, S. Majumdar, J. A. Malen, and A. J. McGaughey, "Coupling of organic and inorganic vibrational states and their thermal transport in nanocrystal arrays," J. Phys. Chem. C **118**, 7288 (2014).
[70]H. R. Seyf and A. Henry, "A method for distinguishing between propagons, diffusions, and locons," J. Appl. Phys. **120**, 025101 (2016).
[71]M. N. Luckyanova, J. Mendoza, H. Lu, B. Song, S. Huang, J. Zhou, M. Li, Y. Dong, H. Zhou, and J. Garlow, "Phonon localization in heat conduction," Sci. Adv. **4**, eaat9460 (2018).
[72]S. Andersson and O. Andersson, "Thermal conductivity, heat capacity, and compressibility of atactic poly (propylene) under high pressure," Int. J. Thermophys. **18**, 845 (1997).
[73]S. P. Andersson and O. Andersson, "Volume dependence of thermal conductivity and isothermal bulk modulus up to 1 GPa for poly (vinyl acetate)," J. Polym. Sci. B: Polym. Phys. **36**, 1451 (1998).